# Corrosion risk and corrosion-induced deterioration of ultra-high performance fiber-reinforced concrete containing initial micro-defects

*Document Version:*
Publisher's PDF, also known as Version of Record (includes final page, issue and volume numbers)

**Please check the document version of this publication:**

• A submitted manuscript is the version of the article upon submission and before peer-review. There can be important differences between the submitted version and the official published version of record. People interested in the research are advised to contact the author for the final version of the publication, or visit the DOI to the publisher's website.
• The final author version and the galley proof are versions of the publication after peer review.
• The final published version features the final layout of the paper including the volume, issue and page numbers.
[Link to publication](#)

Download date: 17. Nov. 2023

# Corrosion risk and corrosion-induced deterioration of ultra-high performance fiber-reinforced concrete containing initial micro-defects

Zhaoping Song [a], Shaohua Li [a], H.J.H. Brouwers [b], Qingliang Yu [a,b,*]

[a] *School of Civil Engineering, Wuhan University, 430072, Wuhan, PR China*
[b] *Department of the Built Environment, Eindhoven University of Technology, P.O. Box 513, 5600, MB Eindhoven, the Netherlands*

## ARTICLE INFO

## ABSTRACT

Micro-defects in UHPFRC, inevitably generated from the manufacturing to engineering service stage, impact its durability under extreme service environments. However, relevant understanding is still insufficient. This work assesses the corrosion risk and corrosion-induced deterioration in UHPFRC containing initial micro-defects, simulated by a combination of mechanical pre-loading and thermal treatment. Analytical analyses include electrochemical tests (OCP, Tafel, EIS), SEM, MIP, compressive strength measurements, etc. Results show that initial defect degree and steel fiber contents have significant effects on the corrosion resistance and mechanical performance of UHPFRC. Micro-cracks and pores are the major channels to deepen fiber corrosion risk, degrading mechanical performance up to 52%-56% in the most severely damaged UHPFRC. The porosity is increased by the corrosion/increased defects and fiber contents up to a growth rate of 35%, 56% and 78%, respectively, as corrosion triggers the occurrence of new defects (e.g., fiber splitting, newborn micro-cracks, pores). The present results provide a reference for predicting the corrosion potential of the defective UHPFRC.

## 1. Introduction

Ultra-high-performance concrete reinforced with steel fibers (namely UHPFRC) is nowadays the most promising material in both civil and military fields thanks to its superior mechanical properties and excellent durability [1–3]. Previous studies have reported that the un-cracked dense matrix with high alkalinity can protect the steel fibers from erosive environmental exposure [4,5], showing a high corrosion resistance in UHPFRC [6,7]. However, cracks generated by damage of thermal and/or mechanical loading exist in almost all reinforced concrete during the service life [8–12], as well as in UHPFRC [13–18]. Such micro-cracks of UHPFRC are inevitable to produce as a consequence of for instance the cases under the pressure of thermal stress caused by cement hydration, especially in large volumes, and loading during service life that impacts the durability over time.

Defects like micro-cracks would initiate fiber corrosion and pose a potential threat to the service performance of UHPFRC. The corrosion development of UHPFRC is obviously different from that of conventional steel-reinforced concrete structures in which limited rebars pass through the matrix that cannot generate an effective circuit due to uneven distribution. The corrosion of UHPFRC would first occur in the fiber

exposed to the surface cover [19], and then the corrosive solution will continue to erode the remaining fibers along the microcracks [20]. Corrosion of steel fiber will inevitably lead to the reduction of its effective interface, and introduce new pores and cracks into the matrix, degrading the mechanical properties of UHPFRC. Therefore, research on the corrosion risk and corrosion-induced deterioration in UHPFRC is of great significance in the long run, considering the factors of the iron nature of steel fiber and the existence of micro-cracks [21].

Some researchers have found that higher steel fiber contents would result in a high corrosion current density [22], inducing greater corrosion risk due to that effective connecting network [23]. Based on an artificial simulation of a single steel fiber, some studies have predicted the corrosion risk via the electrochemical methods [7,24] and characterized the pore changes at the fiber-matrix interface of UHPFRC using images analysis [25]. However, the artificial simulation of a single steel fiber is not sufficient to characterize the corrosion risk and deterioration in UHPFRC, which has more weak interfaces for corrosion resistance due to the multiple steel fibers ranging from 0.5 vol% to 3 vol% [2,26,27]. Most studies focus on the excellent mechanical properties, while only a few studies investigate the corrosion-induced deterioration in UHPFRC [28–30]. Some studies directly apply corroded steel fibers into UHPFRC

---

to study its mechanical performance [8,27], and results show that corrosion facilitates the increase of interfacial friction, even leading to the improvement of mechanical properties. Considering the implication of steel fiber corrosion on its own structure and the surrounding matrix, such results are controversial. Once cracked, fiber corrosion would certainly occur and trigger the surrounding matrix deterioration through the existing open pore, causing deterioration in porosity and strength. Pre-cracked UHPFRC has often been performed to investigate the self-healing process [9,19], other than focusing on the corrosion risk and the deterioration of the damaged UHPFRC. A well-known fact is that cracks and reinforcement-matrix interface are the significant factors affecting reinforcement corrosion in concrete. Defects such that pores generated by air upon high temperature and fibers addition during casting [25] provide erosive channels to contact the steel fiber, inducing fiber corrosion and matrix deterioration inevitably. These limited studies indicate that steel fiber contents and structure defects have significant effects on the corrosion risk and corrosion-induced performance deterioration in UHPFRC. However, quantitative characterization of such effects is still missing and related understanding is highly desired, especially considering the fact that proper international standards are yet not available for UHPFRC.

This work attempts to comprehensively explore the corrosion risk and corrosion-induced deterioration of UHPFRC with initial defects. To achieve this, three steel fiber contents ranging from 1 vol% to 3 vol%, and three types of defects simulated by the combination of mechanical pre-loading and/or heat-treatment, are employed to evaluate the performance of UHPFRC. Scanning electron microscope (SEM) is applied to characterize the microstructure among steel fiber, fiber-matrix interface and matrix of UHPFRC before and after corrosion. TG-DTG and XRD analysis are employed to determine the phase composition. The corrosion risk is revealed by porosity analysis, rapid chloride ion test and electrochemical measurements containing methods of open circuit potential (OCP), Tafel and electrochemical impedance spectroscopy (EIS), revealing the relationship between the initial defects and corrosion risk in UHPFRC. The corrosion of all specimens is achieved by accelerated corrosion in a 10 wt% NaCl solution for 7 days to evaluate the performance deterioration of the corroded UHPFRC. The deterioration caused by accelerated corrosion is characterized by optical observation and strength tests. The mercury intrusion porosimetry (MIP) is used to analyze the pore structure changes before and after corrosion induced by the UHPFRC with random defects.

## 2. Experimental program

### 2.1. Materials and mixture

The raw materials used in this study include P·II 52.5 cement, micro-silica, fly ash, superplasticizer (SP) with a solid content of 30%, water and steel fibers. The Brunauer Emmett Teller (BET) surface area of cement, silica fume and fly ash are 981.2, 1816.3, 847.6 kg/m$^2$, respectively. The chemical composition and specific densities of the powder are detected by the X-Ray Fluorescence (XRF) and gas pycnometer (AccuPyc 1340 II Pycnometer), respectively, as shown in Table 1. The particle size distribution of the used powder materials is tested by using a laser particle size analyzer Bettersize 2000E, shown in Fig. 1 (a). Fourier transform infrared spectroscopy (FTIR) tests are performed to characterize the chemical structures of the used powders with wavenumbers ranging from 4000 to 400 cm$^{-1}$ with a resolution of

2 cm$^{-1}$, presented in Fig. 1 (b).

To investigate the influence of fiber content on the corrosion risk and corrosion-induced deterioration in UHPFRC, a single type of hook fiber ranging from 1 vol% to 3 vol%, are utilized in this study. The geometrical and physical properties of the used fibers are presented in Table 2. The mixture proportion used in this study is shown in Table 3.

### 2.2. Specimens preparation

The designed mixture of prepared specimens is presented in Table 3. The fresh UHPFRC pastes are cast into the mold of 50 × 50 × 50 mm$^3$ and φ100 mm × 50 mm. Four treatment methods are used: (A) standard group, curing in water without stress and heat damage; (B) heat curing without stress; (C) a static stress of 12 MPa applied after demolding, then following with heat damage; (D) a static stress of 60 MPa applied after demolding, then following with heat damage. The gradient heat-curing cycle of groups B, C, D is employed as follows: preheating at 40 °C for 2 h before increasing to 240 °C at a rate of 0.8 °C/min, cured at 240 °C for 14 h, then decreasing to 40 °C at 0.8 °C/min. It is noted that the thermal treatment and/or pre-loading aim to accelerate the generation and development of random cracks in UHPFRC. Both factors are critical for the corrosion risk and corrosion-induced degradation of UHPFRC by generating random damages during the service life. After the above treatment, all specimens are cured in water at room temperature in the laboratory until testing. At least three specimens are prepared for each group.

### 2.3. Corrosion risk determination

#### 2.3.1. Calculate the hydration products and characterize microstructure of UHPCs

Thermal Gravimetric analysis (TG), X-ray diffraction (XRD) and SEM experiments are employed to analyze the influence of initial microstructure damage on UHPFRC.

The samples for TG and XRD analysis are all taken from the inner core of the cube specimens [31]. The anhydrous ethanol solvent exchange method is used to terminate the hydration [32]. The dried samples required for TG and XRD analyses are crushed and ground into 80 μm [31], then placed in the vacuum oven at 40 °C for 24 h [33,34]. TG analyses are conducted by a TA Instruments SDT Q900 analyzer from 30 °C to 1000 °C at a constant heating rate of 10 °C/min in a high-purity nitrogen [35]. A MiniFlex600 X-ray powder diffractometer using Cu Kα radiation (λ = 4.5406 Å) is used to record the XRD pattern of the sample, with scattering angles (2θ) of 10°–60° and a scan speed of 5°/min. After data collection, all XRD patterns can be post-processed through Jade 5.0 software.

TG-DTG curve can be used to further ascertain the hydration products and hydration degree of specimens [36].

$$C_3S + 5.3H \rightarrow C_{1.7}SH_4 + 1.3H \tag{1}$$

$$C_2S + 4.3H \rightarrow C_{1.7}SH_4 + 0.3H \tag{2}$$

$$1.1CH + S + 2.8H \rightarrow C_{1.1}SH_{3.9} \tag{3}$$

Then, based on these reactions, Equations (4) and (5) can be derived to calculate the contents of C–S–H and CH [36,37].

$$C-S-H(\%) = \frac{M_{CSH}}{2.1M_H} \times \Delta m_{CSH} \times 100\% \tag{4}$$

**Table 1**
Chemical composition of powders.

| Substance (%) | CaO | SiO$_2$ | Al$_2$O$_3$ | Fe$_2$O$_3$ | SO$_3$ | MgO | TiO$_2$ | Mn$_3$O$_4$ | LOI | Specific density(g/cm$^3$) |
|---|---|---|---|---|---|---|---|---|---|---|
| P·II 52.5 cement | 64.61 | 19.20 | 4.17 | 3.69 | 3.33 | 1.31 | 0.22 | 0.10 | 2.04 | 2.99 |
| micro-silica | 0.05 | 96.33 | 0.16 | 0.28 | / | / | / | / | 0.88 | 2.23 |
| fly ash | 3.72 | 49.51 | 32.70 | 5.99 | 0.77 | 0.65 | 1.22 | 0.06 | 2.50 | 2.78 |
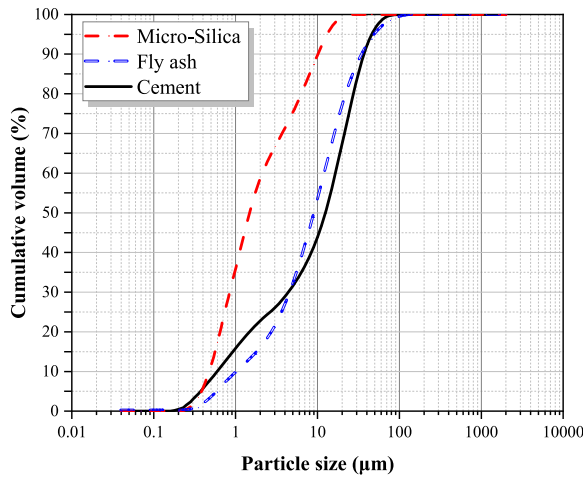
(a). Particle size distribution of powder materials
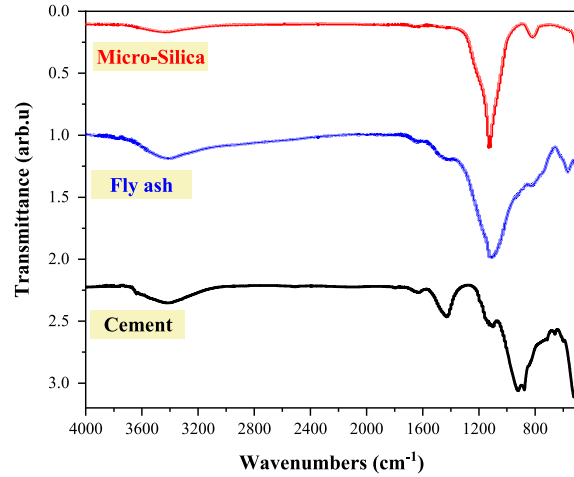


(b). FITR spectra of the used powders

**Fig. 1.** Diagram of the physical and chemical properties of the powder.

**Table 2**
Property of hook steel fiber.

| Diameter (mm) | Length (mm) | Aspect ratio | Density (g/cm$^3$) | Tensile strength (MPa) | Elastic modulus (GPa) |
|---|---|---|---|---|---|
| 0.3 | 25 | 83 | 7.9 | 2500 | 200 |

**Table 3**
UHPFRC paste mixture proportions.

| Quantities | P·II 52.5 cement | Micro-silica | Fly ash | Super-plasticizer | Steel fibers | Water-binder ratio |
|---|---|---|---|---|---|---|
| Mass/ binding powder mass | 0.80 | 0.10 | 0.10 | 0.0075[a] | 1, 2, 3 vol% | 0.18 |

[a] Polycarboxylate-based superplasticizer includes 30% solid and 70% water.

$$CH(\%) = \frac{M_{CH}}{M_H} \times \Delta m_{CH} \times 100\% \qquad (5)$$

where $M_{CSH}$, $M_{CH}$ and $M_H$ represent the molar masses of C–S–H gel, CH and $H_2O$, respectively. $\Delta m_{CSH}$ and $\Delta m_{CH}$ are the mass loss based on the TG curves during 150–400 °C and 400–550 °C, respectively.

### 2.3.2. Porosity and chloride ion diffusion coefficient test

The water-permeable porosity of the designed UHPFRC is calculated through the equation as follows:

$$\varphi = \frac{m_s - m_d}{m_s - m_w} \times 100\% \qquad (6)$$

where, $m_s$, $m_w$ and $m_d$ are the mass of designed UHPFRC measured in the air after saturated for 48 h by vacuum condition, in the water after saturated, and in the air after being kept in oven until a constant weight, respectively.

The determination of rapid chloride migration (RCM) is following the standard NT Build 492 [38]. And the non-steady chloride ion migration coefficient ($D_{RCM}$) of UHPCs is calculated as follows:

$$D_{RCM} = \frac{0.0239 \times (273 + T)L}{(U - 2)t} \left( X_d - 0.0238 \sqrt{\frac{(273 + T)LX_d}{U - 2}} \right) \qquad (7)$$

where $U$ is the absolute value of the voltage (V), $T$ is the average value of the initial and final temperature of the anode solution (°C), $L$ is the specimen thickness (m), $X_d$ is the average depth of chloride ion penetration (m), and $t$ is the test duration (s).

### 2.3.3. Corrosion risk characterization of UHPFRC

The schematic diagram of concrete as a resistance substrate to monitor the corrosion risk of complex multi-steel fibers inside is exhibited in Fig. 2, and the conductive toner and epoxy are pasted to connect the stainless steel sheet and graphite sheet on the concrete surface. The open-circuit potential (OCP), electrochemical impedance spectroscopy (EIS), and polarization curves (Tafel curves) are obtained by connecting the CS Electrochemical Workstation with a computer.

The schematic diagram of OCP, Tafel curve and EIS are shown in Fig. 3 (a ~ c). According to ASTM C876 [39], when the potential is less than −276 mV, corrosion would occur with the 90% probability, shown in Fig. 3 (a). The corrosion rate can be obtained by applying the Tafel polarization curve epitaxy method, presented in Fig. 3 (b). The corrosion resistance can be acquired by EIS, presented in Fig. 3 (c). It is noted that the impedance spectrum of plain concrete is expressed as a single circular arc at high frequency (material arc only with the ion flow in the pore solution, R3); fiber-reinforced cement-based materials are characterized by a double circular arc (material arc incorporating the matrix resistance (R3) occurred at high frequency in which both ion flow and fiber electronic current pass through the matrix, and a medium-high
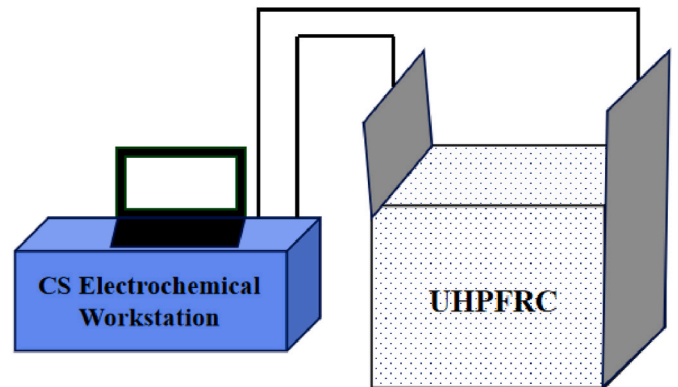


**Fig. 2.** Schematic diagram of concrete as electric resistance matrix to obtain the electrochemical corrosion values.
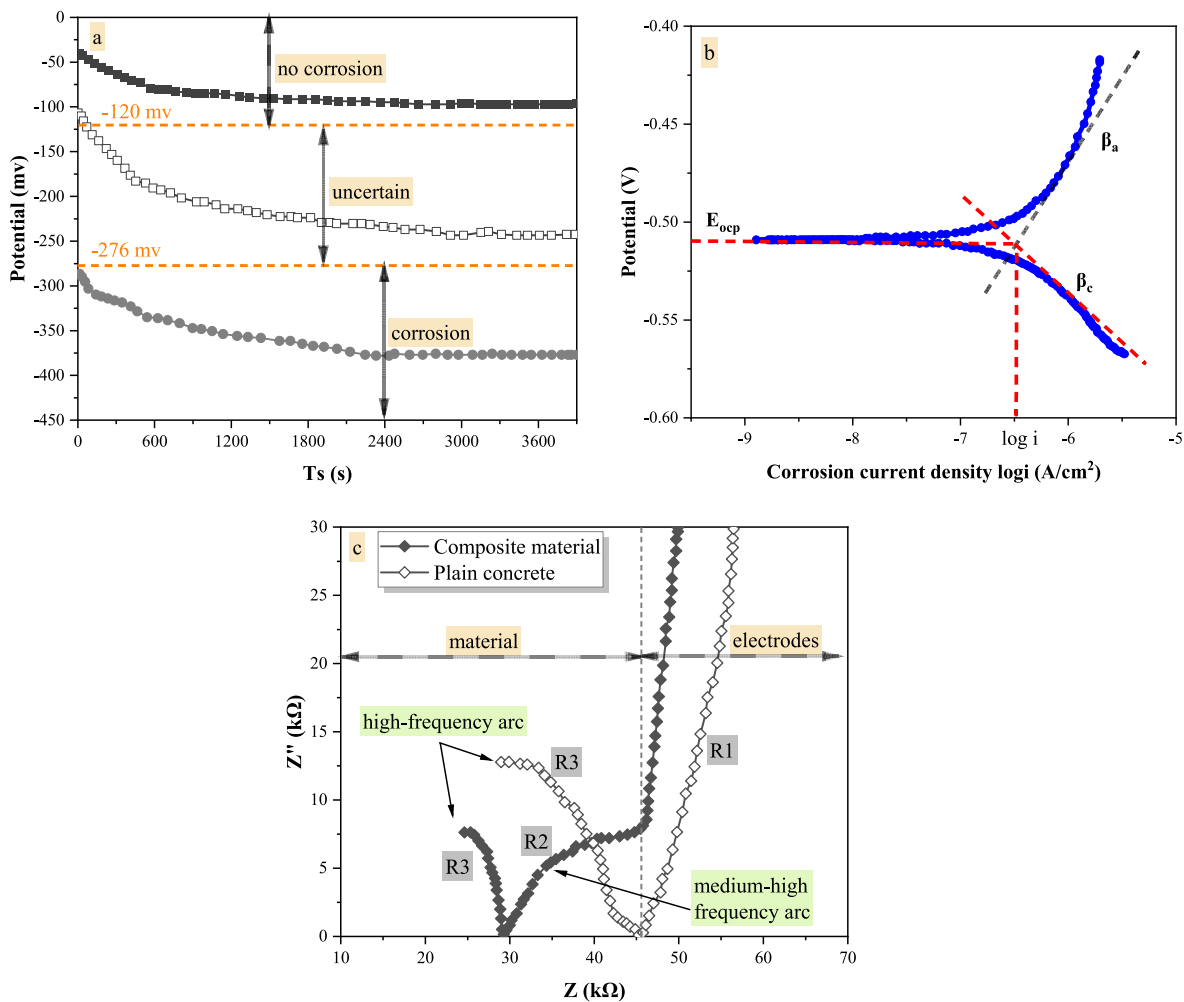
**Fig. 3.** The schematic diagram of (a) corrosion possibility determined by OCP; (b) Typical fitting results measured by Tafel polarization curve; (c) Nyquist scheme of EIS.

frequency arc represents R2 describing the double-layer polarization behavior between steel fiber and the electrolyte). Both stray linear arc at low frequency describes the electrode resistance (R1), shown in Fig. 3 (c). The resistance value of the materials is calculated from the real impedance value between the two arcs.

### 2.4. Corrosion induced deterioration

#### 2.4.1. Accelerated corrosion

Accelerated corrosion test is realized by placing the prepared specimen (coated with conductive material, positive electrode) and stainless steel (negative electrode) in 10 wt% salt solution together. A constant current density at 1.5 A/cm$^2$ is applied to each specimen for 7 days by DC galvanostatic. It is worth noting that such a current density would not occur in the natural engineering, but accelerated corrosion would not change the nature of corrosion [40].

#### 2.4.2. Analysis of matrix damage and mercury intrusion porosimetry (MIP)

The matrix damage of cracking and spalling induced by corrosion can be observed by the actual pictures. The samples are placed on the same plate to record the picture of the corroded UHPFRC, where the same magnification of 2 × is applied for all samples to eliminate the size scale influence. Pore structures of designed UHPFRC before and after corrosion are analyzed by mercury intrusion porosimetry (MIP) of AutoPore IV instrument (Micrometritics). To eliminate the implication of inherent heterogeneity in the cement-based composite material, each

thin mortar sample of 1 cm × 1 cm × 1 cm is randomly taken from at different location in the parent matrix of designed UHPFRC. Then the samples for MIP testing are placed in anhydrous ethanol with a concentration of 99.999% to terminate the hydration. Before testing, they all dried in a vacuum drying oven at 40 °C for at least 48 h.

#### 2.4.3. Compressive strength measurement of UHPFRC before and after corrosion

The analysis of Compressive strength deterioration is conducted on the cubic UHPFRC specimens using an electro-Hydraulic Servo compression machine (YAW-2000kN), in accordance with EN 196–1:2005 [41]. The compressive strength is the average value of three specimens in each group.

#### 2.4.4. Microscopic observation

The micro-structure is evaluated by scanning electron microscopy (TESCAN MIRA3) equipped with an accelerating voltage of 30 kV, which can acquire the image information of corroded steel fiber and fiber-matrix interface. After the accelerated corrosion test, a block of 10 × 10 × 10 mm$^3$ including cross-section is cut from the corroded UHPFRC specimen. Then, the polished block is cleaned with an ultrasonic cleaner applying alcohol, and then placed in an oven for 24 h to dry the sample. Finally, the block surface is coated with gold for SEM observation.

## 3. Results

### 3.1. Initial defects induced changes

Fig. 4 exhibits the influence of steel fiber contents and initial defects on the microstructure of the UHPFRC. It can be found that the microstructure damage (e.g. micro-cracks and pores) shows more aggregated and obvious (Fig. 4 (B1, B2, B3) with the initial defect of heat damage, compared with that without heat damage in Fig. 4 (A1, A2, A3). It can be explained that UHPFRC suffered from medium-high temperature exposure of 240 °C induce a great discordant thermal deformation [15], accompanied by the initiation and propagation of micro-cracks in the matrix. Additionally, when different degrees of preload are applied in the UHPFRC, stress concentration will occur at some isolated points, causing new cracks to occur that will run through the micro-pore, as indicated in Fig. 4 (D2, D3). Obviously, the more initial defects are, the more micro-cracks occur, where the number and width of micro-cracks appear frequently and get largest in Group D subjected to heat-treatment and 60 MPa stress, followed by Group C and B. The interface of fiber-matrix is potentially a weak zone accompanied by additional pores [25,42]. In this case, the more steel fibers, the greater microchannel is produced in the matrix near the fibers. Heat damage and different preload would further promote the development and generation of the micro-cracks around the fibers. It can be seen from the SEM images that the degradation of microstructure in UHPFRC suffered from heat damage and 60 MPa preloading is the most obvious among all the testing series.

To further understand the composition changes upon the initial defects of heat damage and preloading, the XRD spectra and thermal behavior results are presented in Figs. 5 and 6. In Fig. 5, there are still a large number of un-hydrated cement phases, such as $3CaO \cdot SiO_2$ ($C_3S$) and $2CaO \cdot SiO_2$ ($C_2S$) [14,43]. The diffraction peak of C–S–H gel located at about 30° (2θ) and Ca (OH)$_2$ located at 28°, 34°, 43° and 50° (2θ) are both weakened significantly by the heat damage of 240 °C.

From Fig. 6 (a - b), there are three drastic decrease regions of weight loss at 150–400 °C, 400–550 °C and 600–800 °C related to the dehydration of C–S–H, dehydroxylation of Ca(OH)$_2$ and the decarbonization of $CaCO_3$, respectively. Obviously, C–S–H gel and Ca(OH)$_2$ are
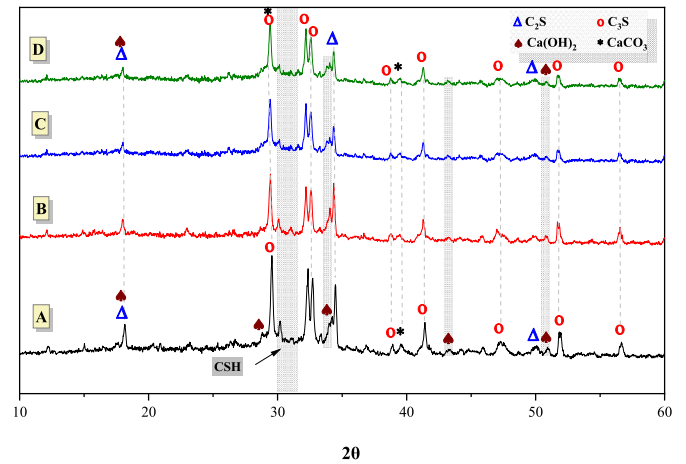


**Fig. 5.** XRD spectra of UHPCs at various initial damage.

decreased with the increase of the heat damage at 240 °C [31]. The contents of C–S–H and Ca(OH)$_2$ in Groups B, C, D following the heat damage and preloading reduce by 7.3%, 14.2%, 16.8% and 29.1%, 28.7%, 24.3%, respectively, compared with that without initial damage (Fig. 6 (c)). The reduction of C–S–H and Ca(OH)$_2$ can be attributed to the following reasons: 1) The hydration reaction of $C_3S$ and $C_2S$ is inhibited due to the heat damage at 240 °C, resulting from excessive water is released irreversibly, causing a decrease on C–S–H gel and Ca(OH)$_2$.2) The hydration reaction is incomplete due to the rapid rate, and the generated C–S–H and Ca (OH)$_2$ quickly wrap the un-hydrated cement particles, resulting in a less generation of C–S–H and Ca(OH)$_2$ than that without heat damage. In addition, Ca(OH)$_2$ is consumed by the accelerated pozzolanic reaction under the medium-high temperature, showing less in Ca(OH)$_2$ compared with C–S–H. 3) Considering that preload provided water-filling space for microcrack [44], it is clear that medium-high temperature will cause a rapid evaporation of the water, which ultimately lowers the generation of C–S–H and Ca(OH)$_2$. Therefore, C–S–H in Group D with heat damage and 60 MPa preload is the
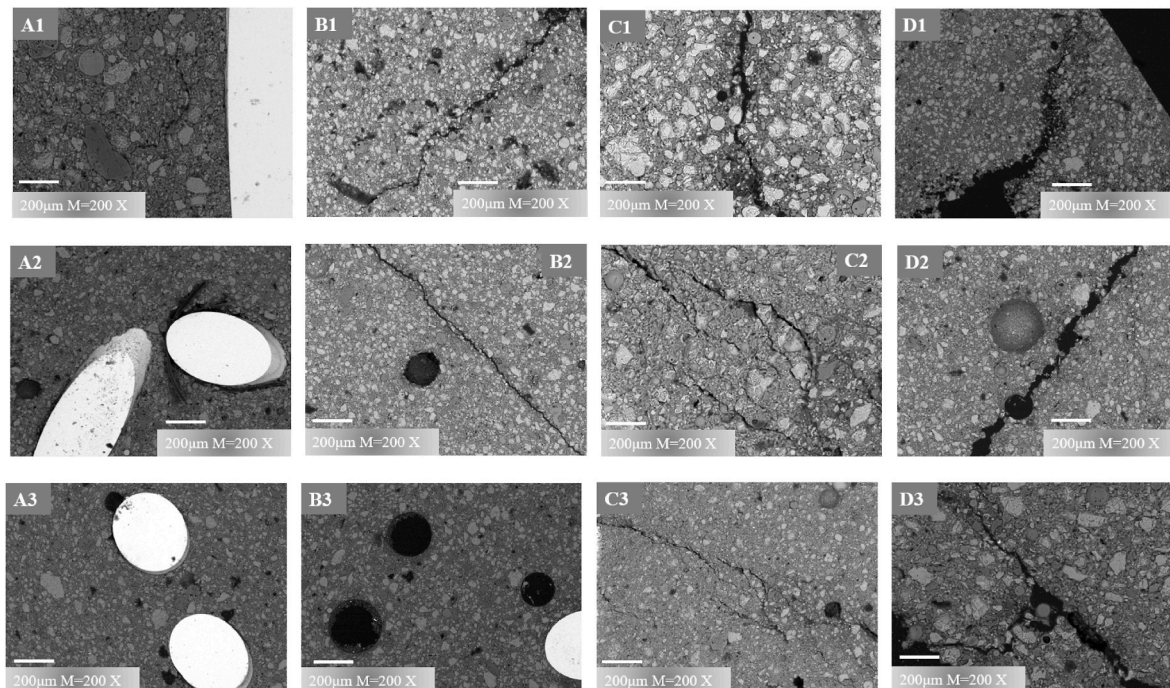


**Fig. 4.** Presentation of actual SEM images on UHPFRC with various initial defects.
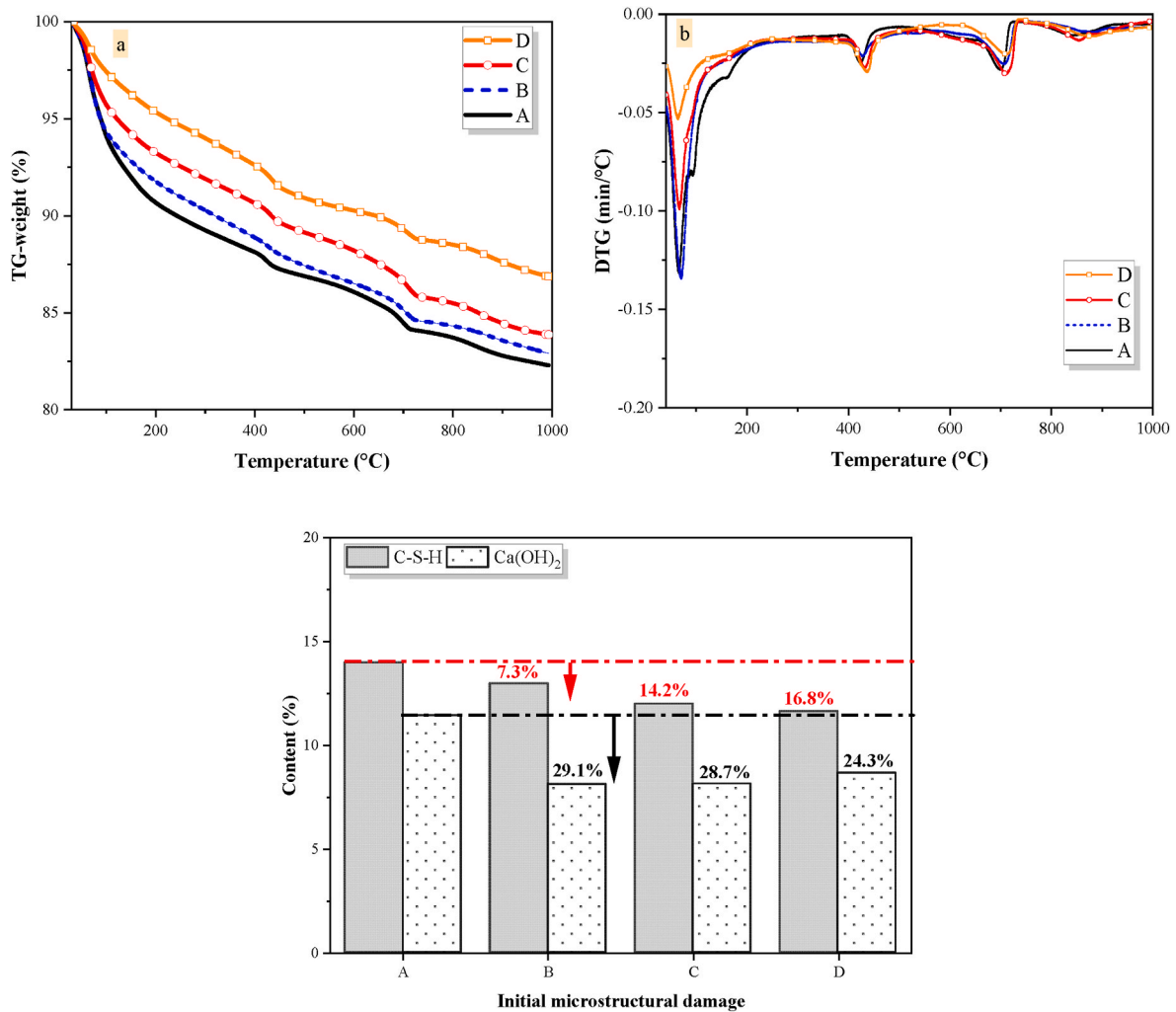
Fig. 6. (a–b) TG-DTG results; (c) C–S–H and Ca(OH)$_2$ contents in UHPCs with various initial damages.

lowest among the all samples.



Fig. 7. Water-permeable porosity of UHPFRC with different initial defects.

## 3.2. Porosity and chloride transport characteristics

Fig. 7 plots the correlations among water-permeable porosity, steel fiber contents and initial defects induced by different simulated method for all designed UHPFRC specimens. It is clear that the value of water-permeable porosity increased with steel fiber content ranging from 1 vol% to 3 vol% under the same initial defects, and increased with the increasing initial defects at the same fiber contents. It could be interpreted by the air-entraining effect as the fiber increases, more physical defects are introduced, leading to the increase in porosity. Also, this confirms that damage development discussed in Section 3.1 is indeed induced by the introduction of steel fibers and the additional external loads, which enlarges additional pores and even more microcracks in the matrix. Regardless of the fiber contents, the porosity of Group D is the largest, followed by Group C and B, while Group A is the smallest. This might be interpreted that the porosity can be influenced by structural defects such as micro-cracks and pores occurred in the UHPCs matrix and around the fibers due to the initial damages.

Fig. 8 (a) and (b) present the impact of initial defects on the changing law of chloride migration in UHPCs. The chloride migration is accelerated with the increasing initial damage and fiber addition (Fig. 8 (a)). It is attributed to that more defects are generated in the matrix and around the steel fibers, caused by air voids entertaining and obvious shrinkage in UHPC itself. Moreover, the mechanical loading accelerates the deterioration of the matrix due to the stress concentration, causing the formation of more micro-cracks, which can act as a transport path for
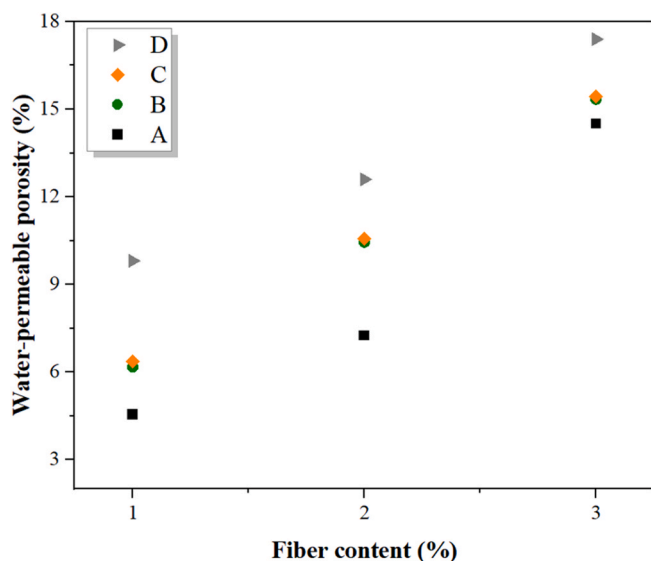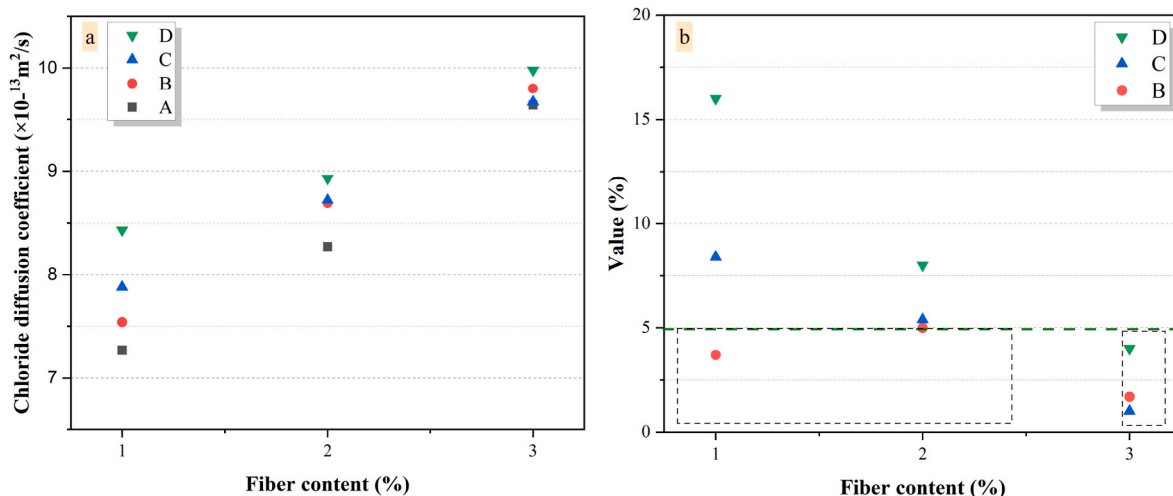
**Fig. 8.** The calculated values, (a) the chloride diffusion coefficient; (b) the growth in other three group, compared with Group An under same fibers.

chlorides [25,45]. A high generation of the micro-cracks enhances the contact area among the pore solution, paste and fibers, consequently accelerating the chloride penetration process. And the three-dimensional disordered distribution of steel fibers forms a dense fiber network skeleton in the UHPCs matrix [22], resulting in a stronger conductivity, which accelerates the transport of chloride ions into the UHPC matrix in the case of an electric current.

Fig. 8 (b) shows a growth value of chloride ion diffusion coefficient in the other three groups compared with Group A under the same fibers. Group B with a slight initial defect than Group C and D shows a small increase less than 5%. When steel fiber reaches 3 vol%, the influence of matrix damage on chloride ion migration is far less than the effect of fiber content, showing less than 5% regardless of the initial defects. This can be explained by that more fibers form a strong electrical conductor, the chloride ion rapidly accesses the matrix and breakdown the passivation layer of steel fiber under the action of applied electricity, causing steel fiber corrosion.

### 3.3. Corrosion risk monitoring of UHPFRC

#### 3.3.1. OCP and polarization curve

The OCP and polarization curve of the designed UHPFRC are presented in (Fig. S1 (a, b), Supplementary information). It can be observed that the potential is gradually reduced with the increased fiber contents and initial defects. From Fig. S1 (b), during the polarization testing at a stable potential (Fig. S1 (a)), it is clear that the corrosion potential tends to shift to the negative direction of Y-axis along with the increase in the corrosion current density, a serious corrosion risk in UHPC will be increased with the increase of fiber contents and initial damage.

The electrochemical parameters obtained from Fig. S1 (b) are presented in Fig. 9, detail in Table S1. It is clear that a higher fiber content results in a higher corrosion density and lower corrosion potential no matter what type of simulated initial defects, due to the conductivity of steel fiber [22]. The early initial damage also has adverse effects on the integrity of the matrix. Obviously, the corrosion current density and corrosion potential in designed UHPFRC of A2, B2, C2 and D2 are 0.2393 $\mu A/cm^2$, 0.2685 $\mu A/cm^2$, 0.3972 $\mu A/cm^2$, 0.6151 $\mu A/cm^2$ and -239 mv, -290 mv, -303 mv and -352 mv, respectively. It can be concluded that micro-crack defects in the matrix provide additional channels for electric current to pass through, resulting in an increase of corrosion current density and a reduction in the corrosion potential, following the order of D > C > B > An under the same fiber content (Fig. 9 and Table S1). Meanwhile, a serious corrosion would occur in UHPC when the corrosion current density is greater than 0.2 $\mu A/cm^2$ and corrosion potential is lower than -276 mv together, while a high risk
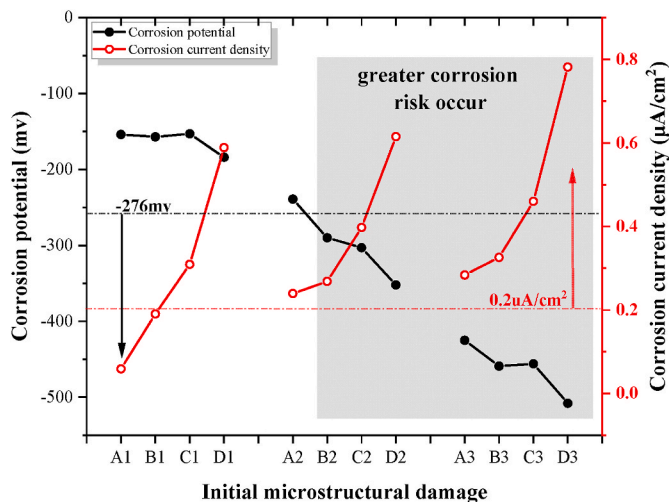


**Fig. 9.** The corrosion potential and corrosion current density in the designed UHPFRC.

of corrosion can be considered when only one of these conditions exists. UHPFRC with no less than 2 vol% and heavy initial damage has a greater corrosion risk. It can be attributed to that steel fiber higher than 2 vol% forms a strong density of the conductive network skeleton. Moreover, the increase of the initial damage strengthens the contact area between the pore solution and steel fiber, leading to a greater risk of rust.

#### 3.3.3. EIS analysis

Fig. 10 (a) shows the original data in the form of Nyquist diagram. The size of the high-frequency arc decreases with the increase of steel fiber amounts and initial defects. This indicates that there is an electrochemical reaction between steel fiber and the ambient matrix, where corrosion products might be generated. With the increase of initial defects and steel fiber content, the low-frequency curve moves closer to the X-axis, indicating that corrosion becomes more serious [46]. A new double-layer polarization at the electrolyte-steel fiber interface is taken place, in the case of the charged ions accumulating on the fiber surface when the current is transferred from the electrolyte in the pore to the steel fiber [47]. It is clear that the greater damage and fibers, the greater contact between the electrolyte and steel fiber, showing a reduction of R3 resistance related to the current including ion flow and fiber electronic current within the pore solution in UHPFRC (Fig. 10 (b)). It should
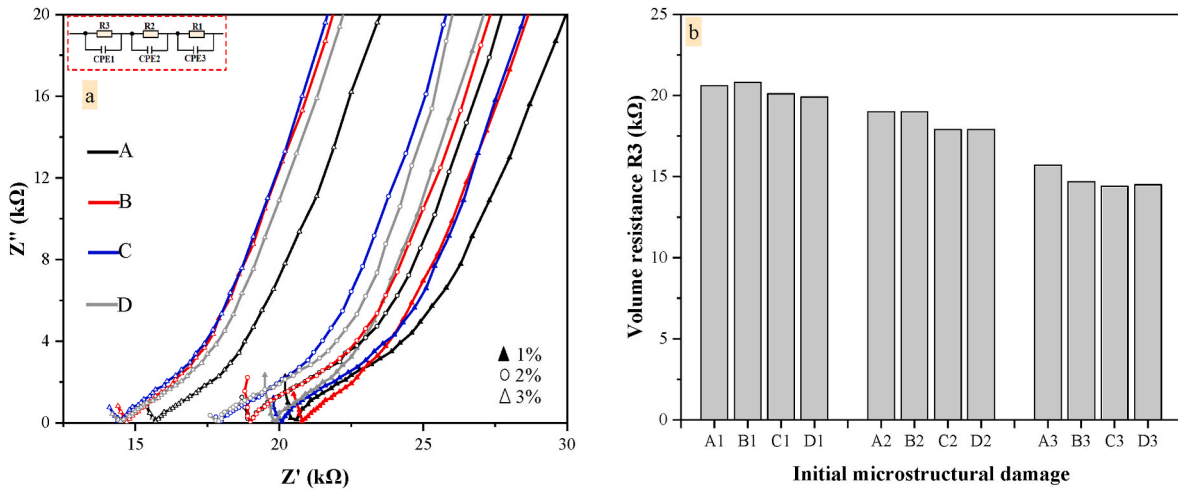
**Fig. 10.** (a) Nyquist scheme; (b) The volume resistance on the designed UHPFRC.

be noted that the effect of electrode resistance (R1) and the second arc (R2) at the medium-high frequency is not the focus of this work, whose stray arc is caused by the polarization effect of sample-electrode interfaces and double-layer polarization behavior of fiber-electrolyte [47], respectively. As shown in Fig. 10 (b), it is apparent that the initial damages cause an obvious reduction in the resistivity compared to Group An under the same fiber content. The resistance reduction in the designed UHPCs of B3, C3 and D3 are gradually reduced by 6.3%, 8.3% and 7.7%, respectively, compared with A3. Both cracks and steel fiber addition will lead to the decline of resistance of UHPCs. The increased steel fiber will sharply increase the current and radically reduce the resistance due to its natural conductivity [22,47]. The existence of cracks provides erosion channels for ion current and electronic current to pass through, showing an increase in corrosion risk.

Fig. 11 presents the relation of R3 volume resistance and corrosion current density of all designed UHPFRC. It is clear that the corrosion current density is continuously increased from 0.0589 $\mu A/cm^2$ to

0.7814 $\mu A/cm^2$ as the initial damages increase under the same fiber amounts. Regardless of the fiber contents, Group D has the highest corrosion current density and lowest volume resistance mainly due to the serious initial damage subjected. The more fiber amount tends to produce higher corrosion current density resulting from its strong electrical conductivity, significantly reducing the volume resistance of UHPCs. Under the condition of heat and stress damage, more micro-cracks are generated, increasing the contact area. Combined with the addition of fibers, more defects are brought into the matrix and connected with the micro-cracks. Under these conditions, the pores are rapidly occupied by ion flow and steel fiber electronic currents. Then, the exchange action between anions and iron ions in the pore solution is strengthened, which further increases the corrosion risk. As such, the mechanical properties of UHPC are degraded due to the fiber corrosion influenced by initial microstructural defects.
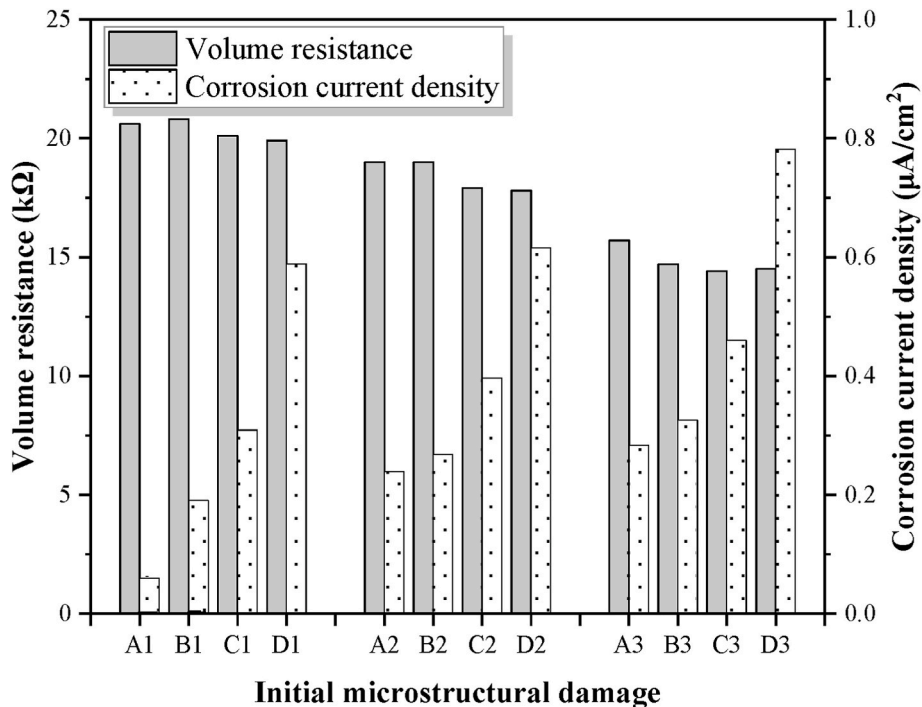


**Fig. 11.** Relation of volume resistance and corrosion current density on designed UHPFRC.

### 3.4. Corrosion deterioration: matrix damage and microstructure alteration

Fig. 12 exhibits the cover damage or even peeling off of the substrate after corrosion of UHPFRC with initial defects. As shown in Fig. 12 (a), when UHPFRC encounters initial defects accompanied by microcracks and pores, the increased steel fiber content accelerates its spalling damage. This is due to that more steel fibers generate an effective strong conductive network, which accelerates the corrosion deterioration developments in UHPFRC under the action of electric fields and erosive solutions. A high fiber content (e.g., more than 2 vol%) would thus greatly impact the corrosion resistance [][23]. The implication of initial defects on the corrosion resistance of UHPFRC is also presented in Fig. 12 (b). It is clear that the cover damage of UHPFRC with initial defects is obviously observed and its deterioration depends with the increasing degree of initial defects. Thus, under the same fiber contents, severe cover damage is observed in D3, and slight damage can be found following the order: C3 > B3 > A3.

Fig. 13 compares the pore size distribution of the designed UHPFRC specimens with and without corrosion measured by MIP test, which can be used to explain the deterioration of mechanical performance. From Fig. 13, the pore size and pore volume of the corroded sample significantly increase with the increased degree of the initial defect and fiber contents, following in the order of D3-after > C3-after > B3-after > A3-after, and D3-after > D2-after > D1-after, respectively. The most significant increment of porosity is in the case of D3 subjected to heat-treatment and most severe preloading, indicating the formation of more microcracks and pores caused by fiber dissolution and corrosion (Fig. 14). This is consistent with the view that the initial damage deteriorates the microstructure and mechanical properties of UHPFRC as described in Sections 3.1, 3.2 and 3.5. For the selected sample of D3-after corrosion, a higher value in pore size, cumulative pore volume and total porosity up to 35% are observed (Fig. 13(c)), compared to the

sample of D3-before corrosion. Further, under the same fiber contents, the porosity shows an increased rate of 3%, 13% and 56% in the corrosion of B3-after, C3-after and D3-after, respectively, compared to A3-after corrosion. As the increased pore size and porosity reduce the transmission resistance of the ion, benefiting the corrosive ions to penetrate into the matrix more easily [48]. The pore size shows an increased trend of 46% and 78% in D2-after corrosion and D3-after corrosion, compared to the D1-after. This might be because the accelerated corrosion dissolves the steel fiber and coarsens the microstructure, together loosening make the matrix. Such a phenomenon could be the vital results of the mechanical deterioration caused by corrosion influenced by the initial defects and fiber contents (Fig. 16).

To further evaluate the status of steel fiber and fiber-matrix interface in the designed UHPFRC, SEM images are observed for samples after being subjected to corrosion as presented in Fig. 14. It is clear that the steel fibers are oxidized severely, and the fiber interface becomes from smooth to rougher even fractured, decreasing the effective area of steel fiber. For the control group (Fig. 14 (A3)), no obvious steel fiber dissolution and visible cracks can be observed, showing limited deterioration. Apart from the incompatible expansion induced by heat stress and external loading stress, new cracks are formed and connected due to steel fiber corrosion. Once subjected to a heavier initial defect, fiber corrosion deepens as a consequence of accelerated corrosion through the existing micro-cracks which provide open channels to erosion. Even the new micro-cracks are generated in the matrix especially near fiber due to the expanding force of fiber corrosion. The deterioration such as the number and width of micro-cracks even fiber dissolution becomes greater with the increased initial defects in the case of the same fiber contents (Fig. 14 (A3, B3, C3, D3)). Under the same initial defects, pores, microcracks and fiber dissolution deepen with the increasing fiber contents (see Fig. 14 (D1-D3)), accompanied with the increase of porosity. Consequently, the mechanical performance of the designed UHPFRC is greatly reduced in the case of Group D with the most severe
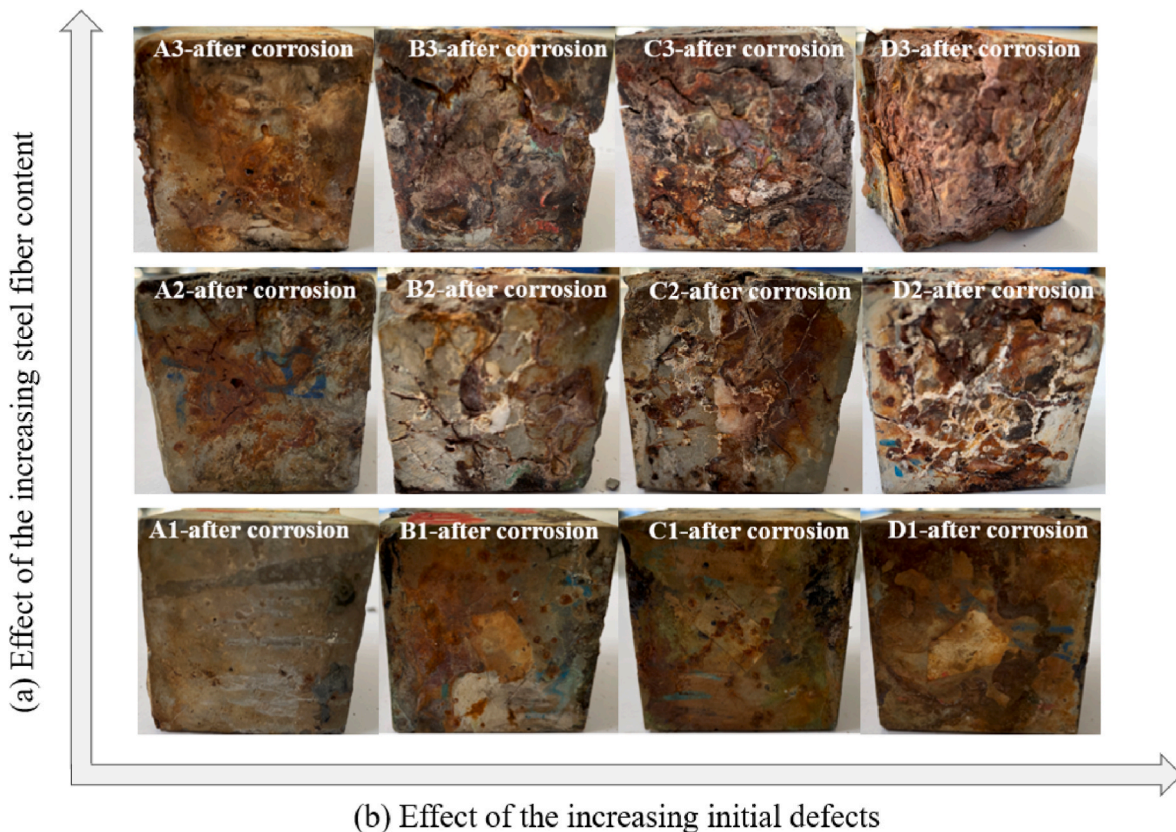


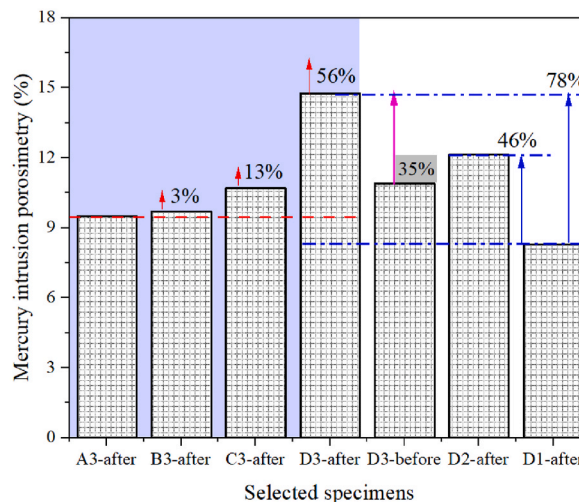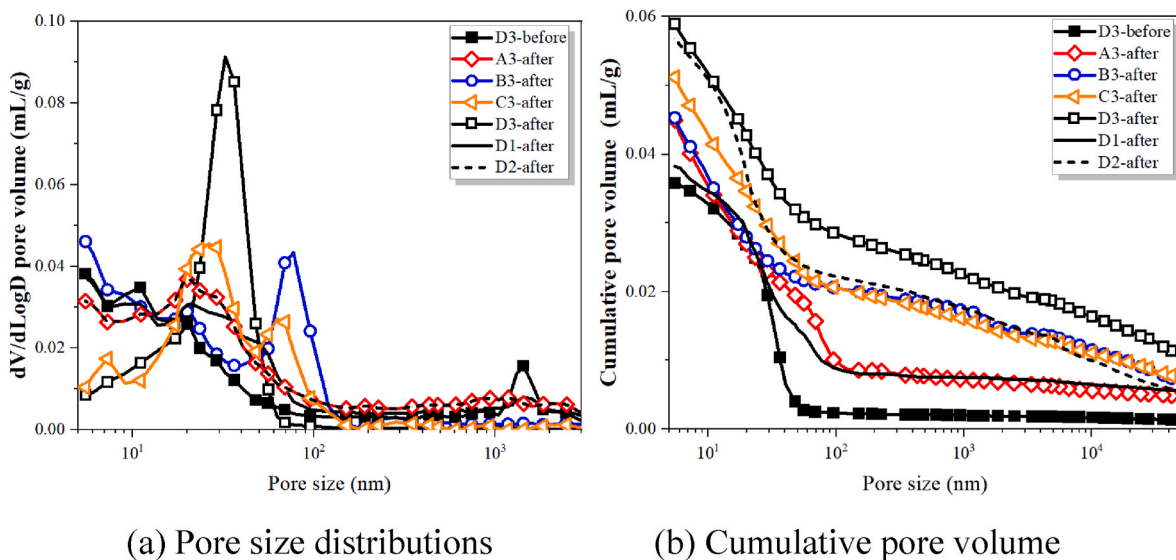**Fig. 12.** Pictures of the designed UHPFRC after subjected to corrosion.

(a) Pore size distributions

(b) Cumulative pore volume



(c) Comparison results of the selected specimens

**Fig. 13.** Results of MIP on designed UHPFRC before and after corrosion.

initial defects.

### 3.5. Strength deterioration caused by corrosion

Fig. 15 plots the quantitative relationship between porosity and compressive strength to further investigate the initial defects-induced performance reduction of the designed UHPFRC before corrosion. Strong relationships in UHPFRC between porosities and compressive strength are found with a highly fitted $R^2$ (0.89–0.99), with different initial defects under the same fiber content from 1 vol% to 3 vol%. Regardless of fiber contents, the compressive strength of UHPFRC before corrosion is followed in the order D < C < B < A according to the degree of the initial defect. The compressive strength before corrosion achieves the highest when the fiber content reaches 3 vol% under the same group initial damages. This is consistent with previous studies [2, 49] that performance increased with the fiber increasing, resulting from that increased stress can be absorbed by the homogenously distributed fibers, consequently preventing the deterioration and propagation of crack.

The results further confirm that heat damage and preload would reduce the compressive strength, resulting from the porosity increased by initial defects. Heat damage would accelerate the occurrence of more

defects due to the serious decomposition of the hydration products, coarsening the pore structure and the degradation of the interface between matrix and fibers [14]. The compressive performance before corrosion of Group B is obviously deteriorated by 7.4%, 5.7% and 4.9% with fiber contents ranging from 1 vol% to 3 vol%, respectively, compared with control Group A. Combined effect of the heat and stress would result in a defective physical structure (e.g., more cracks and pores), causing an obvious reduction in compressive strength. Regardless of the fiber content, the compressive performance of Group D drops severely (Fig. 16). The reduction level is evident with the stress rising, decreasing by 8% for D3, compared with B3. It can be concluded that the strengthening stress in the specimens affects the propagation and expansion of the micro-cracks and pores, when the tensile stress is greater than the tensile strength of UHPFRC, micro-cracks will pass through the pores [50,51], causing the initial damage to worsen. The number and width of micro-cracks will increase with the heat damage and the preload, moreover, more defects are generated near the interface between fibers and the paste, resulting in the deterioration of mechanical properties in UHPFRC.

Fig. 16 exhibits the compressive strength before and after corrosion of all tested UHPFRC specimens with different initial defects. The compressive strength subjected to the accelerated corrosion of control
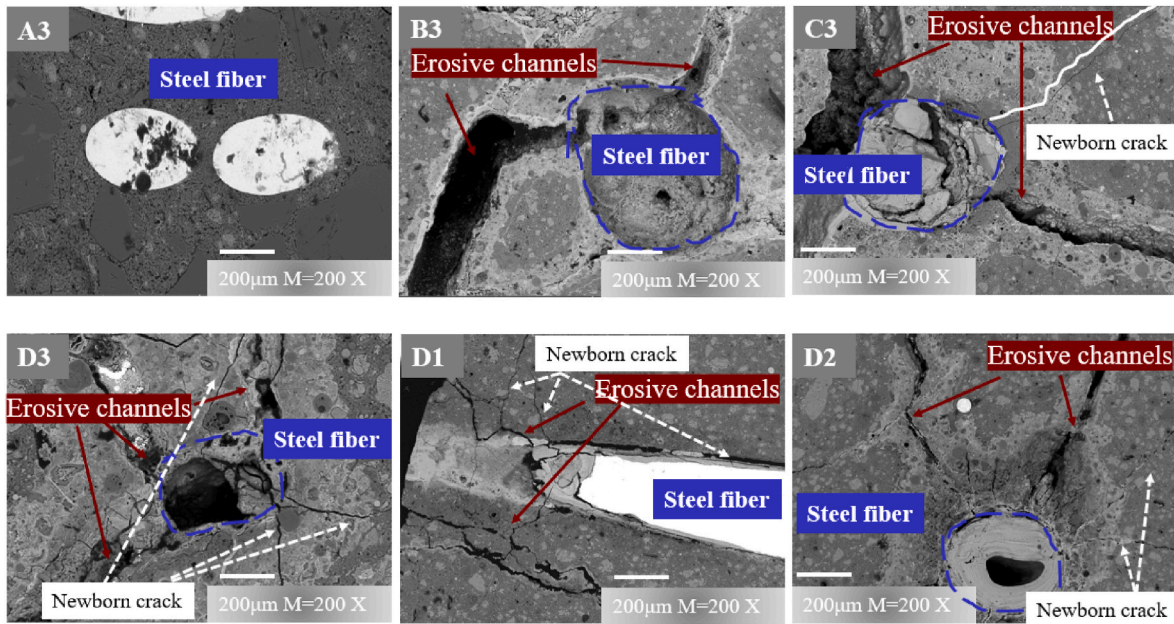
**Fig. 14.** SEM images of steel fiber and fiber-matrix interface of UHPFRC after corrosion (Initial micro-defects act as the erosive channels, and newborn cracks are generated by the expanding force of corrosion products).
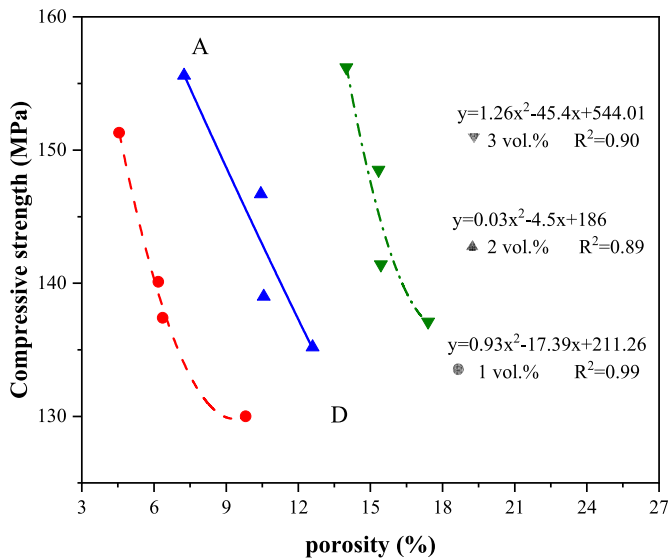


**Fig. 15.** Correlation of porosity and strength on designed UHPFRC before corrosion.



**Fig. 16.** Compressive strength of the designed UHPFRC before and after corrosion.

group A with fiber contents from 1 vol% to 3 vol% are 75-80 MPa, smaller than those (151.3–156.2 MPa) of the specimen before corrosion. The compressive strength decreased by the initial damage and corrosion process, and the fastest decreasing rate of compressive strength after corrosion is found to be more than 50% for the sample of D3 subjected to the largest initial defects. The compressive strength of D3 samples before and after corrosion is 137.1 and 70 MPa, respectively, while the compressive strength subjected corrosion for samples of B3 and C3 is 77 and 73 MPa, respectively. In general, the compressive strength after corrosion shows a decreasing trend with the increase of initial defect degree under the same fiber contents, where all the strengths follow this trend: D < C < B < A. Such mechanical deterioration is due to the fact that the initial defects promote the development of electrochemistry, resulting in corrosion of steel fibers and even fracture or dissolution within the matrix. It has been reported that steel fiber corrosion can be promoted by the action of current and electrolyte solution through the defects of micro-crack and pores. And the multi-fiber is more easily to produce galvanic corrosion, accelerating the formation of corrosion products such that $Fe_2O_3 \cdot nH_2O$ on the fiber surface [8], and decreasing the effective area of steel fiber even the fiber-matrix interface, consequently resulting in the strength deterioration of UHPFRC.

## 4. Discussion

### 4.1. Corrosion risk of UHPFRC with initial defects

The water-permeable porosity can be used to characterize the initial damage in the designed UHPFRC, because it is highly dependent on the development of internal damage (e.g. cracks and pores). Based on this, it is valuable and reliable to use it to describe the microstructure change

and corrosion risk in the designed UHPFRC.

The experimental data and regression curves of correlation among porosities, fiber contents and initial damages are separately plotted in Fig. 17. Regardless of initial defects, the results manifest that the porosities are influenced by the fiber contents in UHPFRC, reflected by clear relationships with excellent $R^2$ (0.98–0.99). It is apparent that the fiber contents would have an unfavorable effect on the porosities in UHPFRC [45]. The current results further certify that the physical defects (e.g. air introduction) increase with the increase of fiber content. This will reduce the matrix compactness, consequently resulting in a parabolic increase of porosity.

It is clear that the corrosion risk of UHPFRC is significantly affected by the microstructure [25] and fiber contents [22], demonstrated in Fig. 18 (a) and (b). Fiber resistance is far less than that of matrix, and it decreases significantly with the increase of fiber content due to the better connectivity and high conductivity [22], ultimately increasing the corrosion risk [22,29]. The porosity increases with the increased damage in the same case of fiber contents, resulting in a slight decrease in the matrix resistance. Clearly, the matrix resistance decreases with increasing porosities due to various initial damages and fiber amounts, and drops sharply with fiber addition. The matrix resistance with 1 vol %, 2 vol% and 3 vol% fibers is 15–16 kΩ, 13–15 kΩ and 11–13 kΩ, respectively.

The corrosion risk of steel fiber-reinforced cement-based material is affected by the fiber contents and the microstructure defects [22,25,52]. A conceptual model concerning porosity/corrosion risk is proposed, presented in Fig. 18 (c). There are obvious defects around the fibers (Fig. 4), and the ITZ of fiber-matrix becomes weaker as the fiber increases [4,25,53]. Electrochemical corrosion process of steel fiber and harmful ions are influenced by the porosities [52]. The greater microstructure damage and fiber content, the more pores and higher corrosion possibility, resulting from that the current in the form of electron flow is more inclined to enter the fiber [54]. Defects caused by micro-structural damage and fiber adding have a twofold influence on the corrosion risk of cement-based materials. Firstly, the matrix defects will affect the $Fe^{2+}$ migration, control the $Fe^{2+}$ concentration, then affect the electrochemical reaction, consequently affecting the fiber corrosion. Secondly, the defect determines the contact area between the fiber and electrolyte [55]. As micro-cracks and micro-voids are formed, more shortcuts for the oxygen, water, and the anions in the solution provide access to the matrix by the electrical migration, and increase the contact surface between harmful substances and fiber-matrix. $Fe^{2+}$ moves through
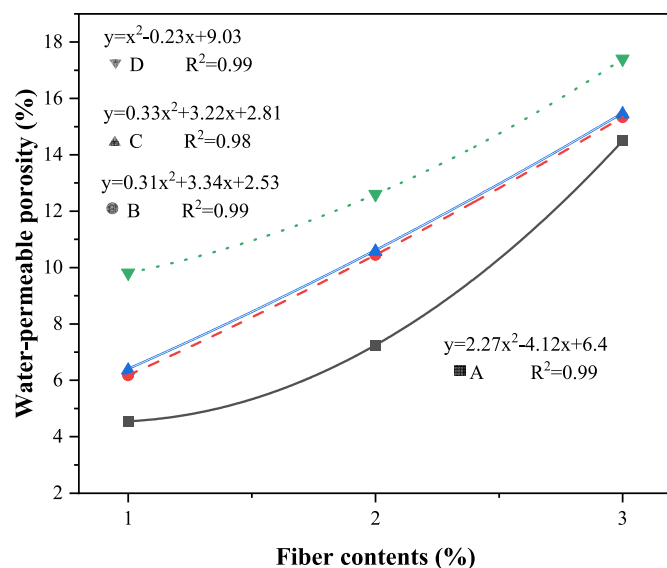
micro-cracks and loosens pore structures, then the unstable $Fe^{2+}$ transform into $Fe^{3+}$. When they are constantly in contact with anions such as oxygen, water and chloride ions in micro-cracks and micro-voids, swapping electrons and reaching equilibrium, the fiber surface is constantly dissolved, resulting in the reduction of corrosion potential. A macroscopic decrease in the volume resistance of samples occurs, consequently increasing the corrosion risk.

### 4.2. Pore structure accelerated corrosion deterioration

This work investigates the initial defects on the corrosion risk and corrosion-induced deterioration in UHPFRC and the results are compared to the control samples without initial damage, where the initial damage is realized by artificial method of heat or loading stress to accelerate the cracks formation. The corrosion risk and corrosion-induced deterioration of UHPFRC are affected by the pore structure and steel fiber contents. The different degrees of damage and steel fiber content lead to varied initial microcracking, pore structure and interfacial bonding strength of steel fiber-matrix in UHPFRC, which determines the corrosion deterioration brought by the generation and aggregation of microcrack. Increased pore structure directly results in the deterioration of mechanical performance in concrete [25], so does UHPFRC, especially when it suffers from initial defects brought by for instance steel fibers addition during the casting process and external damage like thermal or loading induced new micro-cracks during the service life. As described in Sections 3.1 and 3.3, as the damage increases, the fiber-matrix interface becomes weaker and the porosity increases, and the porosity of D3-before corrosion is elevated by 14% compared to A3-before corrosion. Such pores caused by the initial damage and steel fibers addition are equivalent to providing an open pore environment for the aggressive ions from the external environment. When steel fiber corrosion occurs, the internal macropores are likely to appear caused by the gradual dissolution of the steel fibers (diameter 200 μm), and the overall pore size is elevated (see MIP results of Fig. 13 (a) and (b)). As corrosion products continue to increase, the volume expansion pressure generated by the corrosion products continuously squeezes the uncorroded fibers themselves and the surrounding matrix [48], triggering the splitting of the steel fibers (Fig. 14, BSE image of specimen subjected to accelerated corrosion), and even increasing the width of the existing cracks or newborn cracks. As a result, the corrosion rate increases with the increasing contact area between aggressive solution and steel fibers. The steel fibers rapidly encounter electrochemical corrosion, and the fine steel fibers corrode even become new pores, which further increases the porosity, showing a high increase up to 35% in D3-after corrosion compared to D3-before corrosion. This is responsible for the mechanical deterioration of the defective UHPFRC, which leads to approximately 52%–56% reduction in compressive strength.

### 5. Conclusions

The impacts of steel fiber contents and initial defects in UHPFRC on its corrosion risk and corrosion-induced deterioration are investigated in this work. The effects of initial defects on corrosion risk and corrosion-induced deterioration are comprehensively evaluated. This work sheds light on the understanding of corrosion risk and deterioration of the UHPFRC containing initial micro-defects. Based on the experimental results, the main conclusions can be drawn:

- Initial defects combining thermal treatment and pre-loading would cause a larger reduction of 16.8% and 24.3% on the C–S–H gel and Ca(OH)$_2$, increase the porosity by micro-crack and voids, producing a poorer physical structure and deteriorating strength caused by the incompatibility of the thermal and loading stress. With the increasing porosity, chloride migration shows an increasing trend and chloride ions rapidly penetrate the matrix under the action of the
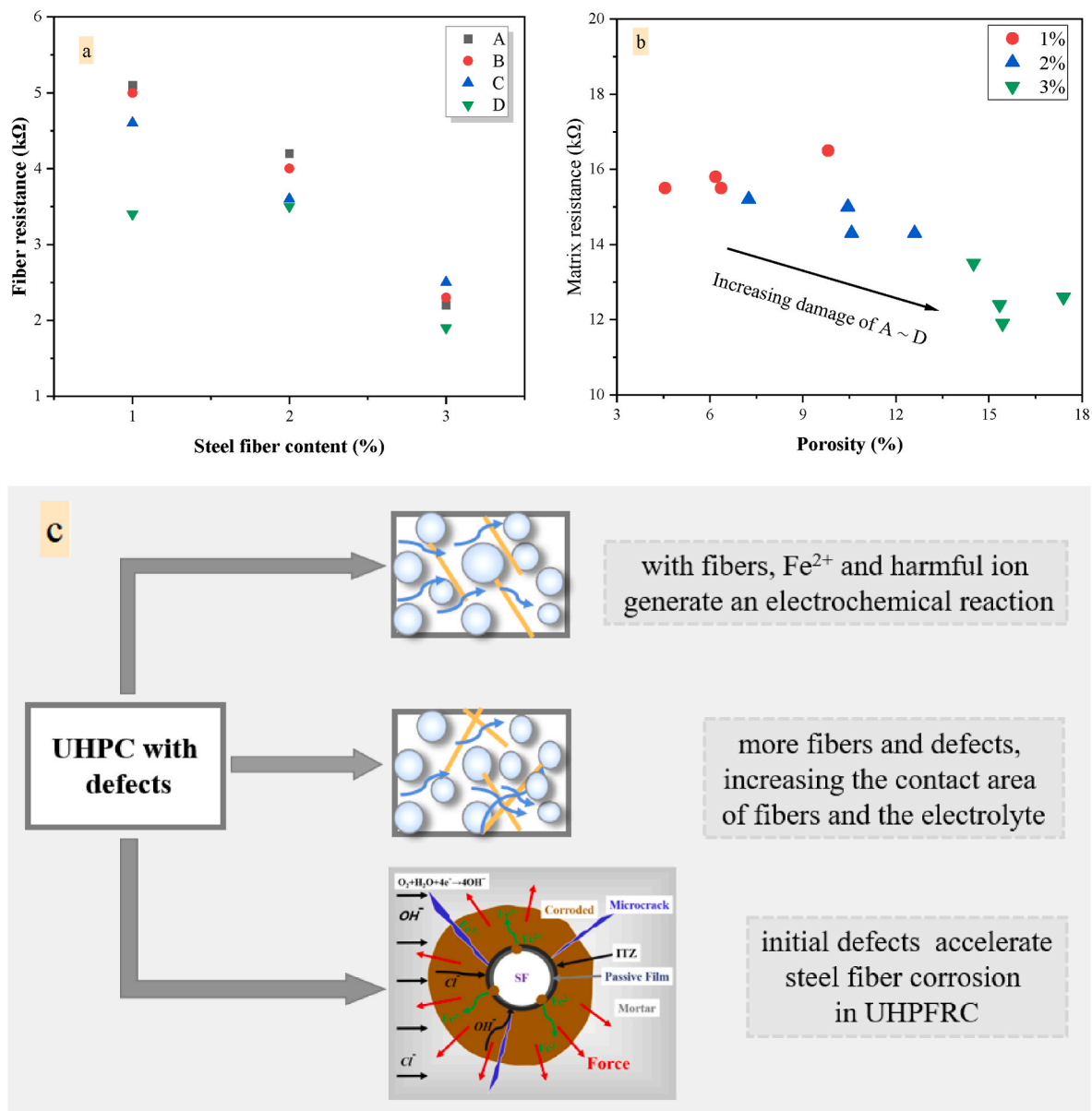


**Fig. 17.** The correlation between water-permeable porosity and fiber content of the designed UHPFRC.

**Fig. 18.** Diagram of, (a) the volume resistance of steel fiber, (b) the relationship of porosity and matrix resistance, (c) schematic representation of UHPFRC with initial defects.

external electric field, and break down the passivation film of steel fibers, causing the corrosion risk.

- The corrosion risk is influenced by the coupling effect of matrix defects and the fiber's conductivity. A higher porosity produced by initial defects and larger fiber content leads to an obvious reduction in volume resistance of UHPFRC, resulting in a greater corrosion risk. All samples with 3 vol% fibers show the highest corrosion risk, especially the samples that suffer from the coupling effect of high-temperature exposure and the most severe mechanical damage.
- The performance of UHPFRC reduces with the increased initial defects, where the compressive strength of the specimen subjected to defects from light to heavy decreases by 5%, 12% and 14%, respectively compared to that without damage at 3 vol%. Moreover, the strength of damaged UHPFRC is notably reduced by corrosive environments: approximately 52%-56% of the compressive strength decreased in the UHPFRC containing initial micro-defects with 3 vol % subjected to the largest pre-loading and heat damage.
- Micro-cracks and pores caused by initial damage are the main channels to accelerate fiber corrosion, and in turn the increased fiber

corrosion leads to an increase in micro-cracks, porosity and ions transport. Under the action of steel fiber dissolution and matrix loosening via the electric field and erosive solution, the porosity of UHPFRC shows a increasing rate up to 35% and pore structure becomes coarser once the occurrence of corrosion. Moreover, the increased fiber contents improve the porosity as high as 46% and 78% in fiber addition of 2 vol% and 3 vol%, respectively, compared to that of 1 vol% subjected to corrosion.

### Declaration of competing interest

The authors declare that they have no known competing financial interests or personal relationships that could have appeared to influence the work reported in this paper.

### Data availability

Data will be made available on request.

## Acknowledgment

This study is supported by the National Natural Science Foundation of China (Grant No. 52178246).

## Appendix A. Supplementary data

Supplementary data to this article can be found online at https://doi.org/10.1016/j.cemconcomp.2023.105208.

## References

[1] Q. Yu, W. Zhuang, C. Shi, Research progress on the dynamic compressive properties of ultra-high performance concrete under high strain rates, Cem. Concr. Compos. 124 (2021), 104258, https://doi.org/10.1016/j.cemconcomp.2021.104258.

[2] D.Y. Yoo, J.H. Lee, Y.S. Yoon, Effect of fiber content on mechanical and fracture properties of ultra high performance fiber reinforced cementitious composites, Compos. Struct. 106 (2013) 742–753, https://doi.org/10.1016/j.compstruct.2013.07.033.

[3] Q. Song, R. Yu, Z. Shui, X. Wang, S. Rao, Z. Lin, Z. Wang, Key parameters in optimizing fibres orientation and distribution for ultra high performance fibre reinforced concrete (UHPFRC), Construct. Build. Mater. 188 (2018) 17–27, https://doi.org/10.1016/j.conbuildmat.2018.08.102.

[4] V. Marcos-Meson, A. Michel, A. Solgaard, G. Fischer, C. Edvardsen, T.L. Skovhus, Corrosion resistance of steel fibre reinforced concrete - a literature review, Cement Concr. Res. 103 (2018) 1–20, https://doi.org/10.1016/j.cemconres.2017.05.016.

[5] R. Yu, Q. Song, X. Wang, Z. Zhang, Z. Shui, H.J.H. Brouwers, Sustainable development of Ultra-High Performance Fibre Reinforced Concrete (UHPFRC): towards to an optimized concrete matrix and efficient fibre application, J. Clean. Prod. 162 (2017) 220–233, https://doi.org/10.1016/j.jclepro.2017.06.017.

[6] M.G. Sohail, R. Kahraman, N. Al Nuaimi, B. Gencturk, W. Alnahhal, Durability characteristics of high and ultra-high performance concretes, J. Build. Eng. 33 (2021), 101669, https://doi.org/10.1016/j.jobe.2020.101669.

[7] H. Zheng, J. Lu, P. Shen, L. Sun, C.S. Poon, W. Li, Corrosion behavior of carbon steel in chloride-contaminated ultra-high-performance cement pastes, Cem. Concr. Compos. 128 (2022), 104443, https://doi.org/10.1016/j.cemconcomp.2022.104443.

[8] D.Y. Yoo, W. Shin, B. Chun, Corrosion effect on tensile behavior of ultra-high-performance concrete reinforced with straight steel fibers, Cem. Concr. Compos. 109 (2020), 103566, https://doi.org/10.1016/j.cemconcomp.2020.103566.

[9] D.Y. Yoo, W. Shin, Improvement of fiber corrosion resistance of ultra-high-performance concrete by means of crack width control and repair, Cem. Concr. Compos. 121 (2021), 104073, https://doi.org/10.1016/j.cemconcomp.2021.104073.

[10] S. Kim, D.Y. Yoo, M.J. Kim, N. Banthia, Self-healing capability of ultra-high-performance fiber-reinforced concrete after exposure to cryogenic temperature, Cem. Concr. Compos. 104 (2019), 103335, https://doi.org/10.1016/j.cemconcomp.2019.103335.

[11] D.Y. Yoo, K.H. Min, J.H. Lee, Y.S. Yoon, Shrinkage and cracking of restrained ultra-high-performance fiber-reinforced concrete slabs at early age, Construct. Build. Mater. 73 (2014) 357–365, https://doi.org/10.1016/j.conbuildmat.2014.09.097.

[12] D. Yoo, J. Park, S. Kim, Y. Yoon, Influence of reinforcing bar type on autogenous shrinkage stress and bond behavior of ultra high performance fiber reinforced concrete, Cem. Concr. Compos. 48 (2014) 150–161, https://doi.org/10.1016/j.cemconcomp.2013.11.014.

[13] J. Li, Z. Wu, C. Shi, Q. Yuan, Z. Zhang, Durability of ultra-high performance concrete – a review, Construct. Build. Mater. 255 (2020), 119296, https://doi.org/10.1016/j.conbuildmat.2020.119296.

[14] H. Huang, R. Wang, X. Gao, Improvement effect of fiber alignment on resistance to elevated temperature of ultra-high performance concrete, Compos. B Eng. 177 (2019), 107454, https://doi.org/10.1016/j.compositesb.2019.107454.

[15] M. Helmi, M.R. Hall, L.A. Stevens, S.P. Rigby, Effects of high-pressure/temperature curing on reactive powder concrete microstructure formation, Construct. Build. Mater. 105 (2016) 554–562, https://doi.org/10.1016/j.conbuildmat.2015.12.147.

[16] K. Habel, P. Gauvreau, Response of ultra-high performance fiber reinforced concrete (UHPFRC) to impact and static loading, Cem. Concr. Compos. 30 (2008) 938–946, https://doi.org/10.1016/j.cemconcomp.2008.09.001.

[17] A.M. Matos, S. Chaves Figueiredo, S. Nunes, E. Schlangen, J.L. Barroso-Aguiar, Durability of an UHPFRC under mechanical and chloride loads, Construct. Build. Mater. 311 (2021), https://doi.org/10.1016/j.conbuildmat.2021.125223.

[18] Y. Wang, J. Li, L. Zhang, L. Zhang, Q. Wang, T. Wang, Structure of the rust layer of weathering steel in A high chloride environment: a detailed characterization via HRTEM, STEM-EDS, and FIB-SEM, Corrosion Sci. 177 (2020), 108997, https://doi.org/10.1016/j.corsci.2020.108997.

[19] D.Y. Yoo, W. Shin, B. Chun, N. Banthia, Assessment of steel fiber corrosion in self-healed ultra-high-performance fiber-reinforced concrete and its effect on tensile performance, Cement Concr. Res. 133 (2020), https://doi.org/10.1016/j.cemconres.2020.106091.

[20] J.L. Granju, S.U. Balouch, Corrosion of steel fibre reinforced concrete from the cracks, Cement Concr. Res. 35 (2005) 572–577, https://doi.org/10.1016/j.cemconres.2004.06.032.

[21] C.G. Berrocal, I. Löfgren, K. Lundgren, L. Tang, Corrosion initiation in cracked fibre reinforced concrete: influence of crack width, fibre type and loading conditions, Corrosion Sci. 98 (2015) 128–139, https://doi.org/10.1016/j.corsci.2015.05.021.

[22] Q. Song, R. Yu, Z. Shui, S. Rao, X. Wang, M. Sun, C. Jiang, Steel fibre content and interconnection induced electrochemical corrosion of Ultra-High Performance Fibre Reinforced Concrete (UHPFRC), Cem. Concr. Compos. 94 (2018) 191–200, https://doi.org/10.1016/j.cemconcomp.2018.09.010.

[23] Q. Song, R. Yu, Z. Shui, L. Chen, Z. Liu, X. Gao, J. Zhang, Y. He, Intrinsic effect of hybrid fibres 3D network on the electrochemical characteristics of Ultra-High Performance Fibre Reinforced Composites (UHPFRC), Cem. Concr. Compos. 114 (2020), https://doi.org/10.1016/j.cemconcomp.2020.103818.

[24] A. Beglarigale, H. Yazıcı, Electrochemical corrosion monitoring of steel fiber embedded in cement based composites, Cem. Concr. Compos. 83 (2017) 427–446, https://doi.org/10.1016/j.cemconcomp.2017.08.004.

[25] J.P. Hwang, M.S. Jung, M. Kim, K.Y. Ann, Corrosion risk of steel fibre in concrete, Construct. Build. Mater. 101 (2015) 239–245, https://doi.org/10.1016/j.conbuildmat.2015.10.072.

[26] L. Teng, W. Meng, K.H. Khayat, Rheology control of ultra-high-performance concrete made with different fiber contents, Cement Concr. Res. 138 (2020), 106222, https://doi.org/10.1016/j.cemconres.2020.106222.

[27] X. Guo, H. Li, S. Wang, Effects of pre-corroded steel fibers on mechanical properties and interface bond behavior of uhpc-normal concrete (nc), SSRN Electron. J. 356 (2022), 129234, https://doi.org/10.2139/ssrn.4143104.

[28] S. Pyo, T. Koh, M. Tafesse, H.K. Kim, Chloride-induced corrosion of steel fiber near the surface of ultra-high performance concrete and its effect on flexural behavior with various thickness, Construct. Build. Mater. 224 (2019) 206–213, https://doi.org/10.1016/j.conbuildmat.2019.07.063.

[29] L.S. Lv, J.Y. Wang, R.C. Xiao, M.S. Fang, Y. Tan, Influence of steel fiber corrosion on tensile properties and cracking mechanism of ultra-high performance concrete in an electrochemical corrosion environment, Construct. Build. Mater. 278 (2021), 122338, https://doi.org/10.1016/j.conbuildmat.2021.122338.

[30] W. Shin, D.Y. Yoo, Influence of steel fibers corroded through multiple microcracks on the tensile behavior of ultra-high-performance concrete, Construct. Build. Mater. 259 (2020), 120428, https://doi.org/10.1016/j.conbuildmat.2020.120428.

[31] L. Alarcon-Ruiz, G. Platret, E. Massieu, A. Ehrlacher, The use of thermal analysis in assessing the effect of temperature on a cement paste, Cement Concr. Res. 35 (2005) 609–613, https://doi.org/10.1016/j.cemconres.2004.06.015.

[32] K. Scrivener, R. Snellings, B. Lothenbach, A Practical Guide to Microstructural Analysis of Cementitious Materials, 2018, https://doi.org/10.1201/b19074.

[33] H. Wang, A. lian Zhang, L. chun Zhang, Q. Wang, Y. Han, J. zhe Liu, X. jian Gao, F. ting Shi, X. yan Lin, L. yu Feng, Hydration process of rice husk ash cement paste and its corrosion resistance of embedded steel bar, J. Cent. South Univ. 27 (2020) 3464–3476, https://doi.org/10.1007/s11771-020-4559-8.

[34] J. Yang, J. Huang, Y. Su, X. He, H. Tan, W. Yang, B. Strnadel, Eco-friendly treatment of low-calcium coal fly ash for high pozzolanic reactivity: a step towards waste utilization in sustainable building material, J. Clean. Prod. 238 (2019), 117962, https://doi.org/10.1016/j.jclepro.2019.117962.

[35] Y.X. Chen, S. Li, B. Mezari, E.J.M. Hensen, R. Yu, K. Schollbach, H.J.H. Brouwers, Q. Yu, Effect of Highly Dispersed Colloidal Olivine Nano-Silica on Early Age Properties of Ultra-high Performance Concrete, 2022, p. 131, https://doi.org/10.1016/j.cemconcomp.2022.104564.

[36] J. Jain, N. Neithalath, Analysis of calcium leaching behavior of plain and modified cement pastes in pure water, Cem. Concr. Compos. 31 (2009) 176–185, https://doi.org/10.1016/j.cemconcomp.2009.01.003.

[37] P.P. Li, H.J.H. Brouwers, W. Chen, Q. Yu, Optimization and characterization of high-volume limestone powder in sustainable ultra-high performance concrete, Construct. Build. Mater. 242 (2020), https://doi.org/10.1016/j.conbuildmat.2020.118112.

[38] J. Lizarazo-Marriaga, J. Gonzalez, P. Claisse, Simulation of the concrete chloride NT build-492 migration test, SSCS 2012 Numer, Model. Strateg. Sustain. Concr. Struct. (2012) 1–8.

[39] ASTM C876, Standard Test Method for Corrosion Potentials of Uncoated Reinforcing Steel in Concrete, ASTM International, West Conshohocken, PA, 2009, 2009.

[40] B. Dong, G. Fang, Y. Liu, P. Dong, J. Zhang, F. Xing, S. Hong, Monitoring reinforcement corrosion and corrosion-induced cracking by X-ray microcomputed tomography method, Cem, Concr. Res. 100 (2017) 311–321, https://doi.org/10.1016/j.cemconres.2017.07.009.

[41] EN 196-1:2005.B. Standard, Methods of Testing Cement, Determination of strength, 2005.

[42] T. Li, X. Liu, Y. Zhang, H. Yang, Z. Zhi, L. Liu, W. Ma, S.P. Shah, W. Li, Preparation of sea water sea sand high performance concrete (SHPC) and serving performance study in marine environment, Construct. Build. Mater. 254 (2020), 119114, https://doi.org/10.1016/j.conbuildmat.2020.119114.

[43] W. Zhuang, S. Li, Q. Yu, The effect of supplementary cementitious material systems on dynamic compressive properties of ultra-high performance concrete paste, Construct. Build. Mater. 321 (2022), 126361, https://doi.org/10.1016/j.conbuildmat.2022.126361.

[44] W. Kurdowski, Cement and Concrete Chemistry, 2014, https://doi.org/10.1007/978-94-007-7945-7.

[45] R. Yu, P. Spiesz, H.J.H. Brouwers, Mix design and properties assessment of ultra-high performance fibre reinforced concrete (UHPFRC), Cement Concr. Res. 56 (2014) 29–39, https://doi.org/10.1016/j.cemconres.2013.11.002.

[46] Shi Jinjie, Sun Wei, Application of electrochemical impedance spectroscopy and X-ray computed tomography to study rebar corrosion in concrete, J. CHINESE Ceram.

Soc. 39 (2011) 1694–1700, https://doi.org/10.14062/j.issn.0454-5648.2011.10.013.

[47] C.G. Berrocal, K. Hornbostel, M.R. Geiker, I. Löfgren, K. Lundgren, D.G. Bekas, Electrical resistivity measurements in steel fibre reinforced cementitious materials, Cem. Concr. Compos. 89 (2018) 216–229, https://doi.org/10.1016/j.cemconcomp.2018.03.015.

[48] W. Xu, Y. Li, H. Li, K. Wang, C. Zhang, Y. Jiang, S. Qiang, Corrosion mechanism and damage characteristic of steel fiber concrete under the effect of stray current and salt solution, Construct. Build. Mater. 314 (2022), https://doi.org/10.1016/j.conbuildmat.2021.125618.

[49] M.A. Ibrahim, M. Farhat, M.A. Issa, J.A. Hasse, Effect of material constituents on mechanical & fracture mechanics properties of ultra-high-performance concrete, ACI Struct. J. 114 (2017) 453–465, https://doi.org/10.14359/51689717.

[50] M. Helmi, M.R. Hall, S.P. Rigby, Effect of pressure and heat treatments on the compressive strength of reactive powder concrete, MATEC Web Conf 147 (2018) 1–7, https://doi.org/10.1051/matecconf/201814701006.

[51] S. Cao, E. Yilmaz, Z. Yin, G. Xue, W. Song, L. Sun, CT scanning of internal crack mechanism and strength behavior of cement-fiber-tailings matrix composites, Cem. Concr. Compos. 116 (2021), 103865, https://doi.org/10.1016/j.cemconcomp.2020.103865.

[52] C. Wen, Y. Tian, Z. Mai, J. Hu, G. Wang, Effect of macropores at the steel-concrete interface on localized corrosion behaviour of steel reinforcement, Cem. Concr. Compos. 129 (2022), 104510, https://doi.org/10.1016/j.cemconcomp.2022.104510.

[53] J.C. Scheydt, Mechanismen der Korrosion bei ultrahochfestem Beton, Karlsruhe Institute of Technology, 2013.

[54] L. Fan, W. Meng, L. Teng, K.H. Khayat, Effect of steel fibers with galvanized coatings on corrosion of steel bars embedded in UHPC, Compos. B Eng. 177 (2019), 107445, https://doi.org/10.1016/j.compositesb.2019.107445.

[55] M. Stefanoni, U.M. Angst, B. Elsener, Kinetics of electrochemical dissolution of metals in porous media, Nat. Mater. 18 (2019) 942–947, https://doi.org/10.1038/s41563-019-0439-8.